Title

Effects of Morphology and Surface Properties of Copper Oxide on the Removal of Hydrogen Sulfide from Gaseous Streams

Journal

Industrial & Engineering Chemistry Research, 58(40)

ISSN

0888-5885

Authors

Azzam, Sara A
Alshafei, Faisal H
López-Ausens, Tirso
et al.

Publication Date

2019-10-09

DOI

10.1021/acs.iecr.9b03975

Effects of Morphology and Surface Properties of Copper Oxide on the Removal of Hydrogen Sulfide from Gaseous Streams

Sara A. Azzam[‡1], Faisal H. Alshafei[‡1], Tirso López-Ausens[1], Richa Ghosh[1], Akash N. Biswas[1], Philippe Sautet[1,2], Sergey Prikhodko[3], and Dante A. Simonetti[1]*

[1]Chemical and Biomolecular Engineering Department, University of California-Los Angeles, Los Angeles, CA, USA 90095

[2]Department of Chemistry and Biochemistry, University of California Los Angeles, Los Angeles, CA, USA, 90024

[3]Materials Science and Engineering Department, University of California-Los Angeles, Los Angeles, CA, USA 90095

*Corresponding Author. Email: dasimonetti@ucla.edu

Keywords: copper oxide, nanomaterials, synthesis, crystallite size, desulfurization, reactive sorption, electrospinning, sorbent

ABSTRACT: This work studies the effects of microscopic shape, crystallinity, and purity for the chemical reaction of CuO nanoparticles with hydrogen sulfide (H_2S) to form copper sulfide. Several CuO nanomaterials were prepared via various synthesis techniques, including sol-gel, precipitation, hydrothermal synthesis in the presence of a polymer/surfactant, hydrolysis, and electrospinning, using different copper precursors (nitrate and acetate) and thermal treatment conditions (623 to 1023 K). The synthesized materials, which had different morphologies (flower-like, nanobelt-like, petal-like, spherical, and nanofibers) and physiochemical chemical properties (e.g., crystallite size, surface area and pore volume), were tested for their performance as low-temperature H_2S sorbents in fixed-bed experiments at 294 K and 1 atm. Despite ostensible differences between the various properties of the tested sorbents, a strong linear relationship was recognized between the sorbents' sulfur removal capacity and crystallite size, independent of changes in the materials' microscopic shape and porosity. Specifically, it was observed that CuO materials with crystallite sizes larger than 26 nm exhibited low sulfur uptake capacities (less than 0.5 wt%) whereas capacity increased linearly (from 0.5 wt% to 12 wt%) with decreasing crystallite sizes for materials with CuO crystallites from 26 nm to 5 nm. In addition, the effect of residual carbon on CuO surfaces was also probed in this study, for the first time, showing that amorphous carbon inherently imparted by the use of a polymer, Polyvinylpyrrolidone (PVP) or poly(ethylene oxide) (PEO), or a surfactant, Poly(ethylene glycol)-*block*-poly(propylene glycol)-*block*-poly(ethylene glycol) (P123), in the synthesis procedure inhibits reaction and deleteriously impacts the H_2S uptake capacity. This trend demonstrates that sorption capacity is strongly influenced by crystallite size and is independent of microscopic shape, surface area and mesopore structure. First principles atomistic simulations explain which surface O anions are most reactive and supportive to the observations.

1. Introduction

Stringent environmental regulations in recent years have required several industries to seek effective and efficient techniques to sequester pollutants present in various chemical conversion processes.[1] Hydrocarbon streams derived from oil, coal, and natural gas processing units are often contaminated by sulfur-containing compounds such as thiols (mercaptans), sulfides, thiophenes, and H_2S.[1,2] These sulfur compounds not only adversely affect the quality and specifications of the product streams but also conflict with health and environmental regulations.[3] Because sour oil and gas reservoirs, which contain high levels of acid gases, are playing a larger role in current energy production technologies due to rising demands for energy and depletion of cleaner petroleum reservoirs,[4] meeting these environmental regulations becomes increasingly challenging with existing processes and technologies.

H_2S is a malodorous and toxic gaseous sulfur compound, which is generated in significant quantities in petrochemical plants across the globe. It causes a wide range of adverse health effects upon inhalation ranging from respiratory irritation to loss of consciousness to death, and its oxidized products (e.g., sulfur dioxide and sulfur trioxide) when released into the atmosphere may have serious, long-term environmental ramifications (e.g., acid rain).[5,6] Additionally, H_2S poses a corrosion hazard on transfer pipelines[4] and downstream equipment, and results in catalyst poisoning (particularly, catalysts containing precious metals, such as, platinum, palladium and rhodium)[7] even when present at low concentrations (1-3 ppm-vol).[8,9]

Because of the chemical affinity of H_2S for metallic cations, chemical reaction with a solid metal oxide is a frequently used technique to purify natural gas from trace levels of sulfide constituents that often remain even after amine scrubbing. Such reactive sorption processes are advantageous because they are thermodynamically more favorable than physisorption leading to

higher purity streams and higher solid phase contaminant capacities. Zn, Fe, Ca, Mn, and V metal oxides have been studied rather extensively in the literature as adsorbents for H_2S removal at elevated temperatures (>573 K).[8,10–16] Despite possessing favorable thermodynamics ($\Delta G_{T=298}$ = 126 kJ mol^{-1}, -76 kJ mol^{-1}, -74 kJ mol^{-1} and -136 kJ mol^{-1} for CuO, ZnO, Fe_2O_3, and NiO, respectively)[17] these oxides when reacted with H_2S at room temperature suffer from low removal capacities due to (1) slow ion migrations to and from the lattice structure, (2) sintering,[18] (3) mechanical disintegration,[18] (4) diffusional resistance,[19,20] and/or (4) limitations in the number of adsorption sites.

Of the previously reported oxides that can remove H_2S at low temperatures, CuO has garnered interest because of the favored sulfidation thermodynamics of Cu^{2+} and Cu^{+1} at room temperature. The high equilibrium constant of CuO sulfidation ($K_s = 6.8 \times 10^{20}$ at 298 K)[21] enables CuO to reduce H_2S from several thousand ppm down to sub-ppm levels. Realizing this advantage, current research efforts have focused on (1) synthesizing small CuO nanoparticles and supporting them on mesoporous materials (e.g., activated carbon, SiO_2, Al_2O_3, clay, and modified zeolites),[22,18,23,24] or (2) combining other metal oxides (e.g., Zn, Fe, Al, V, and Mo-based) with CuO,[19,25,26] to create materials with improved thermodynamic stability and/or kinetics. However, because most of the literature deals with such supported or mixed oxide materials as well as high-temperature H_2S removal processes to avoid kinetic limitations imposed by ambient conditions, little work has been done on unsupported, pure CuO at these milder ambient conditions. Knowledge about several parameters such as the influence of synthesis procedures and crystallite size at low temperatures on reactivity is therefore critical to the use of reactive sorbents in purification processes.

In this work, pure CuO sorbents with varying properties (crystallite sizes, surfaces areas, pore volumes, and purities) and morphologies were synthesized via sol-gel, precipitation, hydrothermal treatment, hydrolysis, and electrospinning, and reacted with 1000 ppm-vol H_2S/N_2 in a fixed bed reactor at room temperature and pressure. The sulfur removal capacity, q_s (g H_2S/100 g sorbent), was estimated by a sulfur mass balance across the reactor. The overall rate parameter, k, was evaluated by analysis of the collected breakthrough curves using a linear driving force model (see SI). Sol-gel, precipitation, hydrothermal treatment in the presence of a polymer, and hydrolysis were used to fabricate CuO nanoparticles with appropriate properties (i.e., small crystallite sizes) for this reaction as the literature indicates that high surface areas, porous structures, and nano-sized particles with small cluster sizes are advantageous for metal oxide desulfurization.[27] Electrospinning, which is a simple, easy-to-use electrostatic fabrication technique, was used to generate one-dimensional Cu-containing nanofibers with varying fiber diameters, which were later thermally treated to remove the polymer matrix and form CuO nanofibers. Different polymers (PVP, PEO and P123) and treatment temperatures (353-823 K) were used to probe the effect of purity (i.e., residual carbon remaining on the surface of the sorbent) on CuO activity. To elucidate information regarding structure-function relationships, the sorbents were characterized using X-ray diffraction (XRD), thermogravimetric analysis (TGA), N_2-physiosorption measurements (BET), scanning electron microscopy (SEM), Energy-dispersive X-ray spectroscopy (EDS) and X-ray photoelectron spectroscopy (XPS). Density functional calculations propose a microscopic origin to the observed size influence.

2. Experimental Methods

2.1 Synthesis methods of pure CuO sorbents

CuO nanoparticles, NP-X, were prepared using an acid-catalyzed sol-gel process.[28] Glacial acetic acid and sodium hydroxide were added, at boiling point, to copper (II) nitrate or copper (II) acetate solution under vigorous stirring. Thermal treatment after vacuum filtration was performed at 623 K, 823 K or 1023 K to achieve different crystallite sizes. CuO nanoparticles (NP-7) and nanobelts (NB-1) were prepared through a precipitation method by a drop-wise addition of aqueous sodium hydroxide solution to aqueous copper (II) nitrate trihydrate solution under continuous mixing. For NP-7, The obtained material, copper (II) hydroxide, was then vacuum filtered, washed and dried. NP-7 precipitates were, then, thermally treated in air at 773 K while NB-1, were treated at 623 K. CuO flowerlike nanostructures, FP-1, were synthesized by hydrolyzing a copper acetate solution at 373 K and then drying the precipitate overnight in air at 353 K.[29] Nanoflake-based flowerlike CuO nanostructures, FP-2 and FP-3, were synthesized via thermally decomposing a $[Cu(NH)_3)_4]^+$ solution, without the aid of surfactants.[30] Copper nitrate was dissolved in deionized water and, then, ammonia was added dropwise. After solution changed color, to dark blue, it was heated to 353 K (FP-2) or 376 K (FP-3) and then a black precipitate was washed, centrifuged and dried.

2.2 Synthesis methods for polymer-assisted CuO sorbents

A set of porous CuO samples, NPC-X, were synthesized according to the method of surfactant-assisted hydrothermal interaction using CuO powder, NP-7, as starting material.[31-33] The polymer-containing solutions were prepared by dissolving different amounts of P123 or PVP (M.W.=1,300,000) in water while stirring. After that, CuO was added under continuous stirring (48 h). The solution was ultrasonically then hydrothermally treated at 383 K in a glass tube reactor (cylindrical pressure vessel) for 24 h. CuO nanofibers, NF-X, were prepared through the electrospinning of a polymer and copper salt solution. Polymer solutions were prepared by

dissolving different amounts of PVP M.W.=1,300,000, PVP M.W.=40,000 or PEO M.W.=300,000 in a solvent (methanol or ethanol) while vortexing. The metal containing solution was prepared by dissolving different amounts of copper (II) nitrate in DI water while stirring. The copper containing solution was then added to the polymer containing solution before undergoing the electrospinning process at different settings. **Table 1** and **2** summarize the conditions associated with each sample while section 1.1 in the supporting information document provides an elaborate account of synthesis details.

Table 1. Physiochemical properties and synthesis procedures of CuO sorbents prepared via sol-gel, precipitation and hydrolysis. [a] Based on XRD. [b] Based on BET. [c] Based on BJH method.

Sample ID	Synthesis method	Precursors	Synthesis/Processing Conditions	Thermal Treatment	Crystallite size (nm)[a]	S_{BET} (m^2g^{-1})[b]	V_{pore} (cm^3g^{-1})[c]
NP-1	Sol-gel	$Cu(Ac)_2.3(H_2O)$, NaOH, CH_3COOH	Vacuum filtration	Dried at 313 K for 8 h	5	14.5	0.040
NP-2			Vacuum filtration	Dried at 313 K for 8 h, then treated at 623 K for 4 h	18	-	-
NP-3			Vacuum filtration	Dried at 313 K for 8 h, then treated at 823 K for 4 h	26	-	-
NP-4			Vacuum filtration	Dried at 313 K for 8 h, then treated at 1023 K for 4 h	53	-	-
NP-5			Centrifuging	Dried at 313 K for 8 h	9	-	-
NP-6			Centrifuging	Dried at 313 K for 8 h	11	-	-
NP-7	Precipitation	$Cu(NO_3)_2{\cdot}3(H_2O)$, NaOH	Vacuum filtration	Dried at 353 K for 14 h, then treated at 773 K for 4 h	18	58.8	0.181
NB-1	Precipitation	$Cu(NO_3)_2{\cdot}3(H_2O)$, NaOH	Aged for 72 h, vacuum filtration	Dried at 333 K for 12 h, then treated at	33	6.18	0.02

				623 for 4 h			
FP-1	Hydrolysis	$Cu(Ac)_2 \cdot 3(H2O)$	Synthesized at 373 for 45 minutes	Dried at 353 K for 12 h	10	-	-
FP-2	Precipitation	$Cu(NO_3)_2.3(H_2O)$,	Synthesized at 353 for 8 h	Dried at 353 K for 12 h	13	-	-
FP-3	Precipitation	$Cu(NO_3)_2.3(H_2O)$	Synthesized at 376 for 24 h	dried at 353 K for 12 h	19	59.1	0.079

Table 2. Physiochemical properties and synthesis procedures of CuO sorbents prepared via hydrothermal treatment, and electrospinning. [a] Based on XRD. [b] Based on BET. [c] Based on BJH method. *weight ratio of polymer used to salt precursor.

Sample ID	**Synthesis method**	**Precursors (polymer: salt)***	**Synthesis/Processing Conditions**	**Thermal Treatment**	**Crystallite size (nm)[a]**	**S_{BET} (m^2g^{-1})[b]**	**V_{pore} (cm^3g^{-1})[c]**
NPC-1	Hydrothermal	CuO (NP-7), P123 (1:1)	Hydrothermal at 383 K for 24 h	Dried at 353 K for 12 h, then treated at 823 K for 4 h Dried at 353 K	21	-	-
NPC-2		CuO (NP-7), PVP (MW=1,300,000) (1:1)			24	17.4	0.05
NPC-3		CuO (NP-7), PVP (MW=1,300,000) (1:9)			18	-	-
NPC-4		CuO (NP-7), PVP (MW=1,300,000) (2:7)			22	-	-
NPC-5		CuO (NP-7), PVP (MW=1,300,000) (2:3)			22	-	-
NF-1	Electrospinning	PEO (MW=300,000), EtOH, $Cu(NO_3)_2 \cdot 3(H_2O)$ (2.7:1)	14 inches, 30 kV, 1.0 cm3/h	Treated at 823 K for 4 h at a ramping rate of 1 K/min	14	-	-
NF-2		PVP (1,300,000), EtOH, $Cu(NO_3)_2 \cdot 3(H_2O)$ (10:1)	15 inches, 35 kV, 5.0 cm^3/h	Treated at 898 K for 10 h at a ramping rate of 0.4 K/min	24	-	-

NF-3		PVP (40,000), EtOH, $Cu(NO_3)_2 \cdot 3(H_2O)$ (2.5:1)	18 inches, 30 kV, 1.0 cm^3/h	Treated at 823 K for 4 h at a ramping rate of 1 K/min	25	-	-
NF-4		PVP (1,300,000), EtOH, $Cu(NO_3)_2 \cdot 3(H_2O)$ (1:1)	6 inches, 20 kV, 1.0 cm^3/h	Treated at 773 K for 2 h at a ramping rate of 2 K/min	40	-	-
NF-5		PVP (1,300,000), MeOH, $Cu(NO_3)_2 \cdot 3(H_2O)$ (1:1)	18 inches, 30 kV, 1.0 cm^3/h	Treated at 823 K for 4 h at a ramping rate of 2 K/min	74	-	-
NF-6		PVP (1,300,000), EtOH, $Cu(NO_3)_2 \cdot 3(H_2O)$ (1:1)	22 inches, 30 kV, 1.0 cm^3/h	Treated at 823 K for 4 h at a ramping rate of 2 K/min	66	2.79	0.002

2.2 Characterization and sulfidation tests

2.2.1 Characterization

The synthesized CuO sorbents prepared via sol-gel, precipitation, hydrothermal treatment, hydrolysis, and electrospinning, as described in Section 2.2 were characterized using a variety of techniques. Powder X-ray diffraction patterns were obtained on an X-ray diffractometer (JEOL JDX-3530 and Philips X-Pert) using Cu Kα radiation of 1.5410 Å to identify the CuO phases. The average crystallite sizes were found using Scherrer's formula. Nitrogen adsorption-desorption isotherms were measured at 77 K with a Micrometrics ASAP 2020 Plus system. Before measurements, the samples were degassed at 1×10^{-3} Torr and 573 K. The Brunauer-Emmett-Teller (BET) surface areas were calculated from the isotherms by using the BET equation. The pore size distribution was derived from the adsorption branches of the isotherms using the Barrett-Joyner-Halenda (BJH) model.

Scanning electron microscopy (NOVA 230 Nano SEM) was used to determine the morphology of the sorbents. The mean diameter and size distribution (standard deviation) of the

electrospun nanofibers were calculated from the SEM micrographs using ImageJ software (n = 250; where, n is the number of fibers that were measured and averaged). Microstructure of the particles was imaged using scanning transmission electron microscope (STEM) Titan (Thermo Fisher Scientific) operating at 300 kV and equipped with the X-Max^N 100TLE (Oxford) detector for energy dispersive spectroscopy (EDS) analysis. Windowless EDS detector was used with high counts rate to optimize the detection of light elements. Samples were prepared by direct deposition of the dry powder onto the carbon film supported TEM grids. EDS spectral maps of individual particles were acquired with the pixel size 2.5 nm in continues mode. Maps were stopped after satisfying elemental images were attained with full map acquisition time varied between 10-20 min. Line scan profile results of individual particles were generated from acquired spectral images.

Thermogravimetric analysis was conducted in a Perkin Elmer TGA. Alumina crucibles were used to hold the samples. Gas flowrates were set to 200 standard cm^3 min^{-1} to minimize external diffusion from the bulk gas to the sample interface. Heating/reaction occurred in air (Matheson UHP Argon, 99.999% purity) at a ramping rate of 10 K min^{-1}. XPS was conducted with PHI 3057 spectrometer using Mg Kα X-rays source at 1286.6 eV. All binding energy values presented in this paper were charge corrected to C 1s at 284.8 eV. For the interpretation of the spectra, the literature positions were applied.[34]

2.2.2 Fixed bed sulfidation experiments

Reactive adsorption of H_2S was studied in an apparatus with plug-flow hydrodynamics shown schematically in **Figure S1**. Copper (II) oxide samples (120-200 mg) were sieved to 75-155 μm agglomerate diameter and packed between plugs of quartz wool in a 0.25-inch outer diameter tubular, stainless steel reactor. Flow rates of gaseous H_2S and N_2 (65 sccm) were introduced to

the packed reactor via mass flow controllers (MKS GE50A and GM50A). Feeds to the reactors consisted of 1000 ppm-vol H_2S in N_2 and were produced by diluting a 1.0% H_2S (Praxair UHP) in N_2 mixture with UHP N_2. All the sulfidation tests were carried at ambient temperature and pressure. The compositions of feed and effluents were monitored using online gas chromatography (Agilent 7890B) with a sulfur chemiluminescence detector (SCD; Agilent 755) and continuous gas phase FTIR spectroscopy (MKS Multigas). All gas transfer lines and the interior of the reactor were treated with an inert coating (SilcoNert 2000) to mitigate H_2S adsorption onto tubing walls.

2.3 Computational study

Section 3.2 of this work features a computational study using Density Functional Theory (DFT) for the reaction mechanism of the dissociative adsorption of H_2S molecules on CuO {111} surfaces. This surface was picked because it is the most stable surface[35] found experimentally. It should be noted that the data shown in section 3.2 regarding computational work corresponds to a short account of an upcoming work carried out by our group which will be published eventually.

The dissociative adsorption of H_2S on a CuO surface involves several elementary steps, i.e., the molecular adsorption of H_2S on the surface, with subsequent dissociative steps, rearrangement of adsorbed species and formation of water, which overall corresponds to the stoichiometric reaction:

$$CuO + x\ H_2S \rightarrow CuO_{1-x}S_x + x\ H_2O$$

The net balance of the process is the exchange of one oxygen atom of the CuO surface by one sulfur atom provided by H_2S. The reaction mechanism was studied by determining the relevant stationary points for all the elementary steps, along with the potential energy surface (PES), using DFT together with a planewave basis set as implemented in the VASP code.[35-38] Exchange

and correlation effects were treated within the generalized gradient approximation (GGA), using the Perdew–Burke–Ernzerhof (PBE) functional along with projector augmented-wave pseudopotentials.[39] Potential van der Waals interactions were considered by using the dDsC correction as implemented in VASP.[40] The planewave basis set cutoff was set to 450 eV. A Monkhorst-Pack scheme was used for sampling the Brillouin zone.

Due to the failure of conventional DFT functionals to properly account for the strong correlation effects among the partially filled Cu 3*d* states in CuO.[41] The Hubbard parameter, U, was introduced for the Cu 3*d* electrons to describe the on-site Coulomb interaction (GGA+U). Specifically, the values of U=7 eV and J=0 eV were adopted from the literature.[42,43]Upon optimization of a bulk CuO unit cell to agree with experimental lattice parameters and the proper anti-ferromagnetic character, a CuO {111} model surface featuring a 2x1 CuO {111} supercell was built using the slab approach. The dimensions of the supercell were 11.6 Å x 6.1 Å, with a slab thickness of 7 Å and a vacuum region in the Z axis of 19 Å to avoid spurious electrostatic interactions between supercell instances. The model used can be seen in **Figure S8**.

3. Results and Discussion

3.1 Physio-chemical properties of CuO materials

XRD was used to identify the crystalline phases and average crystal sizes of the nineteen CuO sorbents prepared in this work, using the synthesis techniques described in Section 2.1 and the SI. As shown in **Figure S2**, all the XRD patterns collected show diffraction peaks which are characteristic of the planes of a single-phase monoclinic CuO. The average crystal domain size of the CuO sorbents calculated using Scherrer's formula based on the 38.8º peak were in the range of 5 to 74 nm, with the majority of the sorbents having crystallite sizes less than 25 nm (**Table 1-2**). The XRD results show that, in general, sorbents that did not undergo thermal

treatment in air at elevated temperatures (T > 773 K) as part of their preparation technique had significantly smaller crystallite sizes (< 20 nm). This effect is important to highlight because it was observed in this work that crystallite size influences the H_2S removal capacity of pure CuO sorbents, irrespective of other properties (such as, surface area, pore size, and pore volume) generated by the synthesis technique (discussed in detail in Section 3.2). Furthermore, the d-spacing obtained from the XRD data for all sorbents was in the range of 2.29-2.30 Å for the (200) plane, which is consistent with the literature[44], and indicative of phase pure monoclinic CuO.

Figure S2(d) also shows the XRD patterns of the as-synthesized NF-1 (PEO-$Cu(NO_3)_2$) and NF-4 (PVP-$Cu(NO_3)_2$) prior to any thermal treatment. Well defined diffraction peaks are absent from the XRD pattern of the pre-thermally treated NF-4 fibers, which indicates that these materials consist of amorphous PVP phases and copper species that are too small to diffract X-rays. Moreover, the XRD patterns of NF-1 (prior to thermal treatment) contains several small peaks consistent with PEO as well as copper nitrate peaks reported previously in the literature.[45,46] These results indicate that thermal treatment in air is required for the formation of CuO from the copper-species that exist in PEO or PVP nanofibers after electrospinning.

N_2-physiosorption was performed on one sample from each of the morphologically distinct groups (NP-4, NP-7, NB-1, FP-2, NPC-2 and NF-6) to determine the effect of synthesis method on surface area and porosity. **Table 1** and **Table 2** show the structural parameters calculated from nitrogen adsorption and **Figure S3** shows the pore distribution curves. Analysis of structural parameters along with the degree of micro- and meso-porosity reveals differences in surface area and porosity among the sorbents. Specifically, sorbents that were prepared via precipitation (NP-7 = 58.8 $m^2 g^{-1}$ and FP-3 = 59.1 $m^2 g^{-1}$) possessed larger BET surface areas than

those prepared from sol-gel (NP-1 = 14.5 $m^2 g^{-1}$), hydrothermal treatment (NPC-2 = 17.4 $m^2 g^{-1}$), and electrospinning (NF-6 = 2.79 $m^2 g^{-1}$). CuO nanobelts appear to be an exception to this observation with a surface of area 6.18 $m^2 g^{-1}$ which can be attributed to the long aging step (72 hours) in the synthesis procedure which can lead to micropore and mesopore closure. Additionally, NP-7 (precipitation) had pore volumes of 0.181 $cm^3 g^{-1}$ which is more than double that of FP-3 (0.079 $cm^3 g^{-1}$) despite their comparable surface area. These differences in total pore volume are the result of different pore size distributions (**Figure S3(b)**). NP-7 consists of a larger concentration of pores in the 15 to 150 nm pore size range compared to FP-3, which has higher pore volume within the lower pore size range > 15 nm (**Figure S3(a)**). In general, changes in pore volumes followed the same trend as for the surface area (i.e., samples with smaller pore volumes also exhibited lower surface area). The significantly lower surface area and low meso-porosity of the electrospun materials result from the formation of single CuO fibers with large intra-fiber interstices as determined by SEM (**Figure 1h**).

SEM was used to investigate the effect of preparation technique on the morphology of the synthesized materials. **Figure 1** shows the SEM images (20,000 times magnification) of the representative CuO materials synthesized in this work--Nanoparticle samples: NP-1, NP-5, NP-7; Nanoparticles synthesized with polymer: NPC-1; Nanobelts: NB-1; Flower-shaped particles: FP-2, FP-3; and Nanofibers: NF-4. These SEM images reveal that various CuO morphologies and dimensionalities can be obtained by simply varying the preparation technique. **Figure 1 (a-b)** shows that nanostructures prepared via sol-gel (NP-1, NP-5) were found to have irregular particle shapes with varying domain sizes depending on the copper precursor (average domain size of 4.5 ± 1.47 μm for copper (II) acetate in **Figure 1(a)** and 1.3 ± 0.4 μm for copper (II) nitrate NP-5).

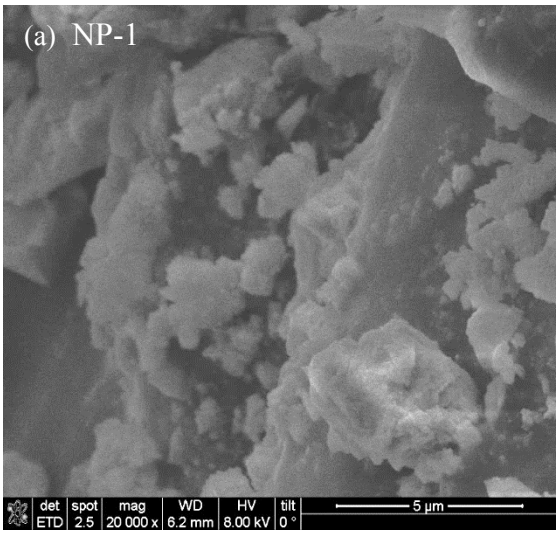
(a) NP-1
det spot mag WD HV tilt
ETD 2.5 20 000 x 6.2 mm 8.00 kV 0 °
5 µm

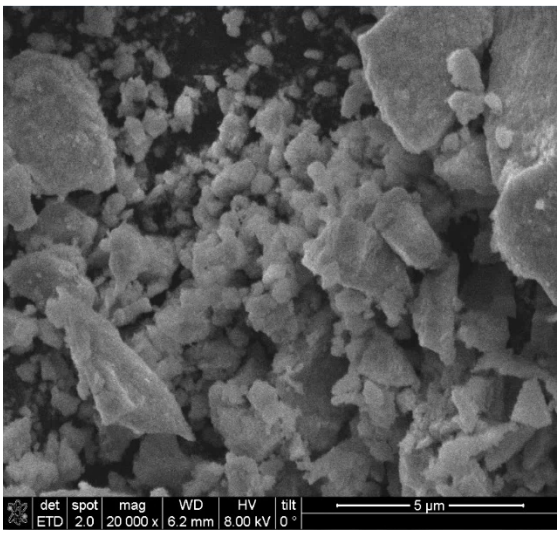
det spot mag WD HV tilt
ETD 2.0 20 000 x 6.2 mm 8.00 kV 0 °
5 µm

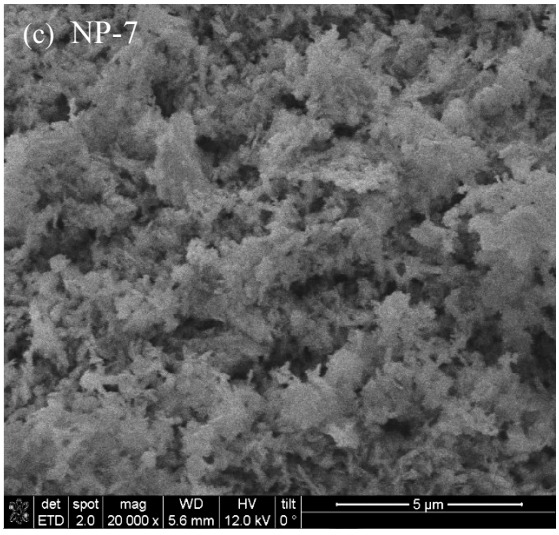
(c) NP-7
det spot mag WD HV tilt
ETD 2.0 20 000 x 5.6 mm 12.0 kV 0 °
5 µm

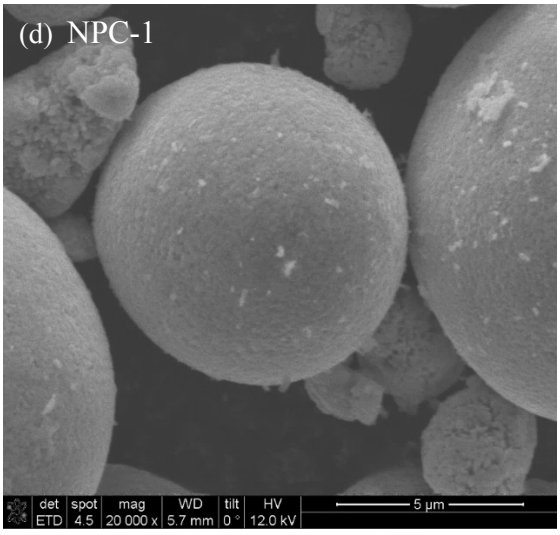
(d) NPC-1
det spot mag WD tilt HV
ETD 4.5 20 000 x 5.7 mm 0 ° 12.0 kV
5 µm

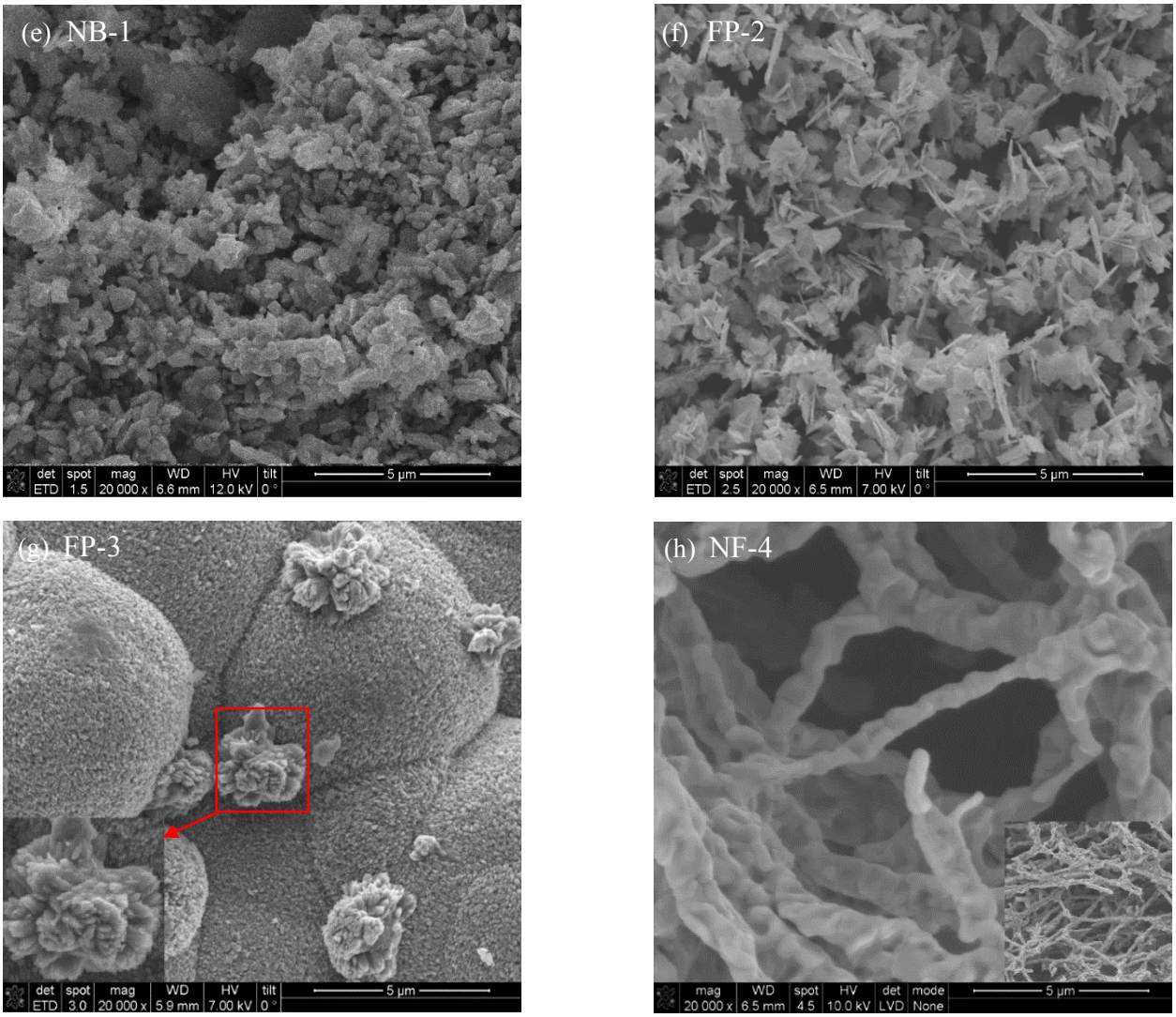

Figure 1. SEM images at 20,000 times magnification of a select group of CuO sorbents with different morphological features prepared via various synthesis techniques (e.g., sol-gel, precipitation , hydrothermal treatment with the aid of a polymer, hydrolysis, and electrospinning), as described in **Section 2.2**, **Table 1** and **Table 2**.

Unlike sol-gel, which yielded materials that were irregular in shape, precipitation, hydrothermal treatment and electrospinning, yielded materials with regular, defined shapes and structures. For instance, by hydrothermally treating NP-7 (**Figure 1(c)**) in the presence of P123 (NPC-1), closely aggregated and distinctly spherical CuO particles were formed, with sizes

ranging from 5 to 9 μm as seen in **Figure 1(d)**. Properly aging a precipitated CuO sample (NP-7) lead to nanobelt-like materials as shown in **Figure 1(e)**. The effect of reaction time and metal concentration on precipitation of flowerlike particles (FP-2 and FP-3) can also be observed in **Figure 1 (f-g)**. As the reaction time and copper precursor concentration were increased, flowerlike structures formed (**Figure 1(g)**), with an average size of 2.7 ± 0.9 μm. At low concentrations and temperatures, however, instead of forming these micron-sized flowerlike structures, petal-like structures are formed (0.5-2 μm) (**Figure 1(f)**).[47] Lastly, **Figure 1(h)** shows how electrospinning can result in the fabrication of a highly porous, fibrous structure, with significant macro-porosity (NF-4). The fibers formed via electrospinning (NF-4) after undergoing thermal treatment had an average diameter size of 629 ± 194 nm (measured using ImageJ, n=250). The SEM images, indeed, confirm that different synthesis techniques yield nanomaterials with markedly different morphological features while also shedding light on the growth mechanism of CuO nanostructures as a function of synthesis condition.

TGA experiments were conducted on pure PEO (M.W.=300,000), pure PVP (M.W.=1,300,000), and NF-4 (prior to thermal treatment; PVP-$Cu(NO_3)_2$) to quantify the extent of polymer removal during thermal treatment (i.e., quantity of residual carbon left after treatment) and provide evidence of the conversion of copper nitrate to CuO. **Figure 2** shows the TGA curves of pure PEO, pure PVP, and NF-4. All three samples were decomposed under air at a heating rate of 10 K min^{-1}. The nanofibers synthesized using pure PEO (M.W.=300,000) decomposed under air in a single step, with a total weight loss of approximately 99%. The TGA results prove that at the 823 K, the majority of the PEO polymer is removed. The nanofibers synthesized using pure PVP (M.W.=1,300,000), on the other hand, decomposed under air in two

steps, with a total weight loss of approximately 93.7% at 773 K, 94.2% at 823 K, and 94.7% at 897 K, which is a slightly lower weight loss percentage than PEO (**Figure 2**).

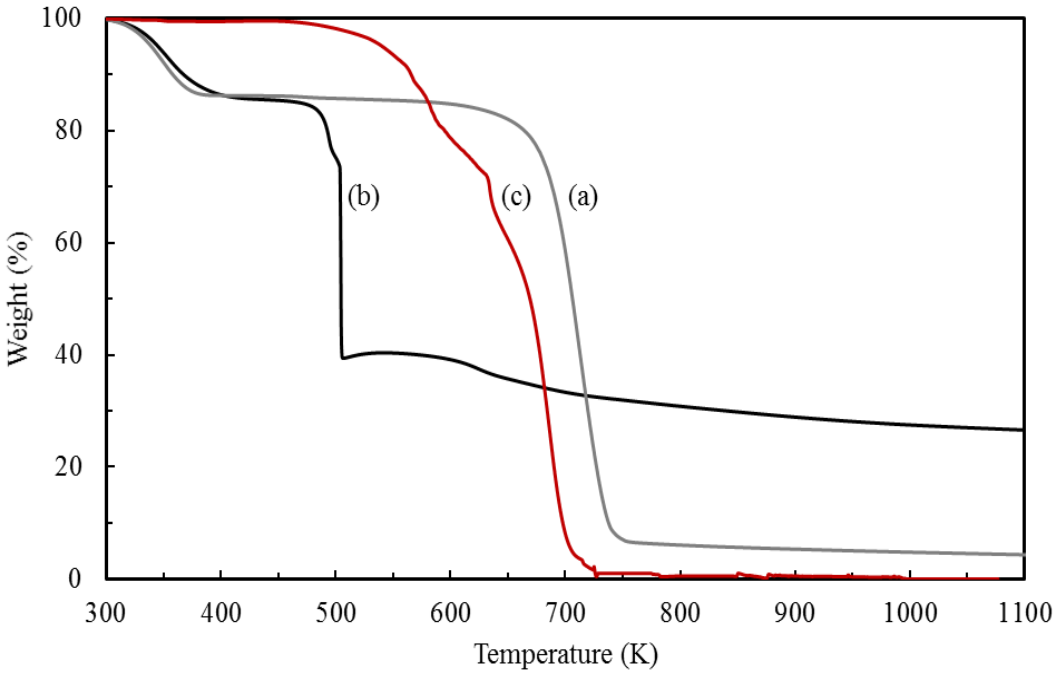

Figure 2. Weight loss profiles as a function of temperature from thermogravimetric analysis (TGA) of (a) pure PVP (M.W.=1,300,000), (b) NF-4 prior to thermal treatment (PVP-$Cu(NO_3)_2$), and (c) pure PEO (M.W.=300,000) nanofibers.

In the case of PVP, the first step weight loss of 16% occurred between ambient temperature and 622 K and was attributed to the evaporation of volatile solvents. The second step weight loss of 78% from 623 K to 773 K was attributed to the thermal degradation of the PVP chains. It is clear from the TGA curve that the majority of the PVP matrix (much like in the case PEO) is removed at temperatures higher than 773 K and only a small amount of carbon residue is left, albeit this amount of carbon residue is slightly higher in the case of PVP (due to the presence of more carbon atoms in the PVP monomer than in PEO). The work of Borodko et al. further supports the presence of residual carbon after the thermal treatment of PVP at elevated

temperatures.47 Using spectroscopic techniques, the authors studied the degradation of PVP and showed that in an oxygen atmosphere, the PVP forms a polyamide-polyene-like material at temperatures above 523 K. At temperature above 573 K, these materials transform into amorphous carbon. Lastly, NF-4, an electrospun nanofiber sample consisting of PVP (M.W.=1,300,000) and $Cu(NO_3)_2$, decomposed under air in two steps, with a total weight loss of approximately 84% (**Figure 2**). These total weight losses in air are consistent with the complete conversion of copper nitrate to CuO. Thus, the first step weight loss can be attributed to the evaporation of volatile solvents, and the second can be attributed to the decomposition of the PVP chains and the conversion of copper nitrate to CuO. **Figure 2** also reveals that the decomposition of NF-4 (475 K) occurs at a much lower temperature than pure PVP (640 K) indicating the effect of copper nitrate, which weakens the bonds within the PVP chains, and of the nitrate anions, which act as an oxidant to combust the polymer. These TGA results are in agreement with the results from the other characterization techniques described in this section, as they provide quantitative evidence of the removal of the majority of the polymer (PEO or PVP), decomposition of the copper nitrate, and formation of CuO during the thermal treatment of electrospun nanofibers (e.g., NF-4) in air while also hinting at the presence of small amounts of amorphous carbon remaining in the sorbent after thermal treatment of the as-synthesized fibers.

To further probe the presence of carbon and quantify its amount on the surface of the oxide sorbents, X-ray photoelectron spectroscopy (XPS) experiments were performed. **Figure 3** shows the overall XPS spectra as well as the spectra of the C 1s core level for a select group of sorbents (NP-7, NPC-2, and NF-4).

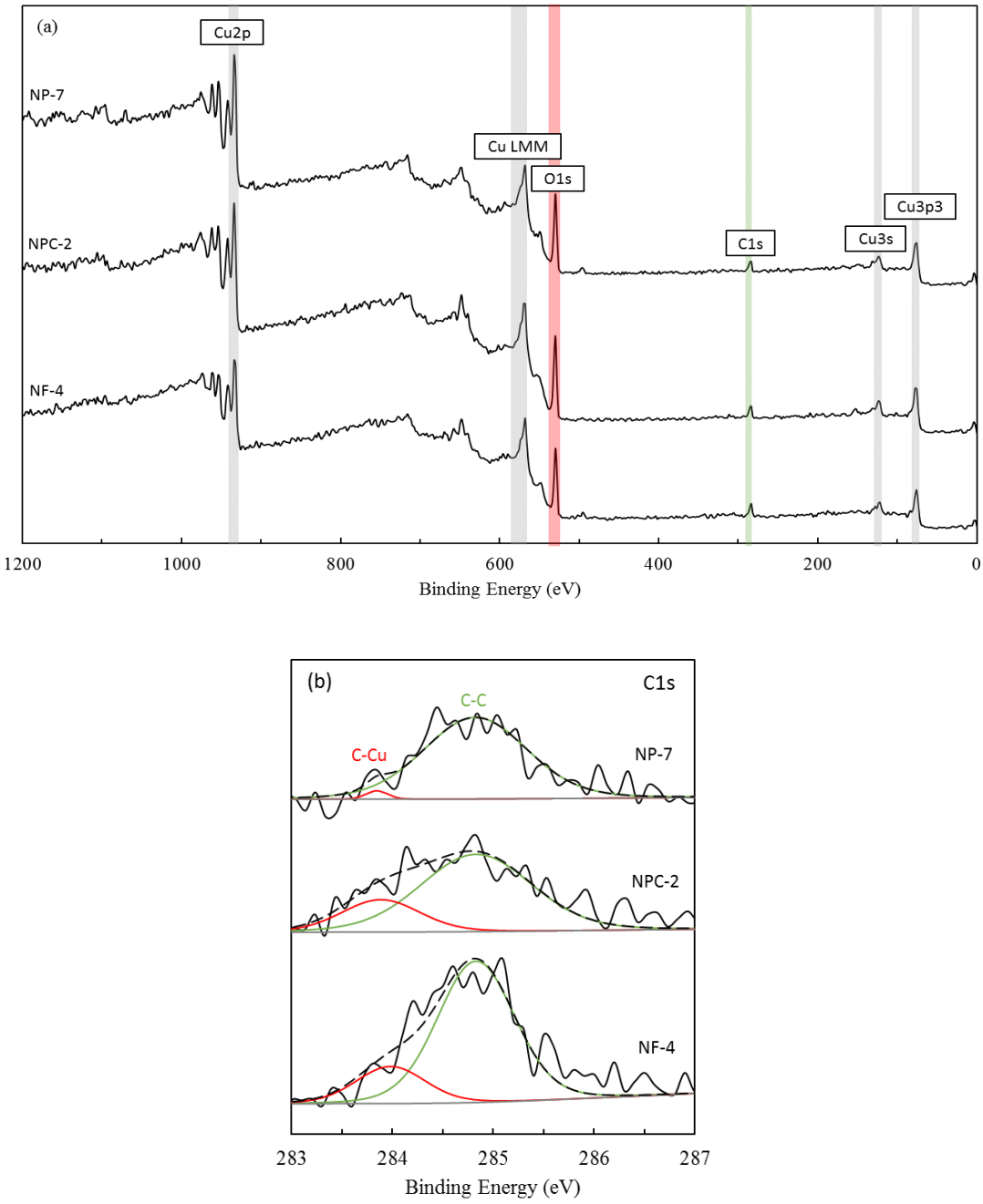

Figure 3. XPS spectrum of CuO nanomaterials (NP-7, NPC-2, and NF-4) prepared via precipitation (no polymer), hydrothermal treatment in the presence of PVP (M.W.=1,3000,000), and electrospinning, using PVP (M.W.=1,300,000) as a template, respectively. (a) Wide spectra of the copper oxide sorbents, (b) high-resolution spectra of C 1s, with peak fittings corresponding to C-C and C-Cu.

As mentioned in Section 2.2 and Table 1, NP-7 was a CuO sorbent that was prepared via precipitation , NPC-2 was a CuO sorbent that was prepared by hydrothermally treating NP-7 in the presence of PVP (M.W.=1,300,000), and NF-4 was a CuO nanofibrous sample that was synthesized using electrospinning from a copper nitrate precursor in the presence of PVP. In the case of both NPC-2 and NF-4, the weight ratio of PVP to Cu added during synthesis was 1:1 whereas no polymer was added in the case of NP-7. The XPS results reveal the presence of CuO nanocrystals, as shown by the Cu 2p3/2 peaks in **Figure 3**, for all three sorbents. The binding energy of the Cu 2p3/2 peaks was found to be 933.6 eV, which is in agreement with the literature.[48-50] Additionally, the intensities of the Cu 2p shake-up peaks obtained from the CuO sorbents is close to the ratio characteristics of reference CuO.[34] **Figure 3(b)** shows the C 1s spectra for three selected CuO sorbents. In **Figure 3(b)**, the C 1s peak has the highest intensity, demonstrating the presence of carbon. The main carbon peak at 284.8 eV corresponds to the C-C bonding (all three sorbents contain this C-C bond) while the shoulder at 283.3 eV corresponds to the C-Cu bonding energy, which is mainly due to the carbon residue remaining on the surface of the sorbent after thermal treatment. Fitting results of the C 1s high-resolution XPS spectra were used to quantify the amount of C-Cu present in each sorbent. The fittings reveal that NPC-2 and NF-4 contained 22% and 19% C-Cu, respectively, whereas NP-7 contained less than 2% C-Cu. XPS results for other samples, summarized in **Figure S4**, show a variation in surface C-Cu percentage ranging from 19% to 50%. The XPS results discussed in this section signify the impact of synthesis (i.e., the utilization of a polymer or a surfactant) on the amount of residual carbon (C-Cu) present in the sorbent which is important for the evaluation of sulfur removal performance.

3.2 Effect of crystallite size on H_2S removal

To probe the effect of morphology and crystallite size on H_2S removal performance, the capacities of the sorbents synthesized in this work for H_2S removal were measured during fixed bed experiments. The capacities are defined as g H_2S per 100 g of sorbent (wt%) where complete sulfidation of CuO corresponds to 42 wt%. Capacities were determined by introducing a feed with a nominal concentration of 1000 ppm-vol H_2S in N_2 and monitoring the H_2S concentration in the reactor effluent (as described in Section 1.1 of the SI). Experiments were terminated after the concentration of the effluent was equal to the inlet concentration, and H_2S capacities were calculated from the mass differential between the inlet and outlet of the reactor over the course of the experiment.

The capacities were plotted as a function of surface area, total pore volume and microscopic domain size, **Figures S5(a-c)**, but no apparent correlation was observed between capacity and any of these parameters. In contrast, **Figure 4** shows that H_2S capacity is inversely proportional to crystallite size (from a range of 5-26 nm) regardless of synthesis procedure and thus, regardless of morphology, surface area, and pore structure. Samples with crystallites >26 nm exhibited similarly low capacities (0.4-0.5 wt%) across a broad range of sizes (26-75 nm). These results indicate CuO crystallite size is the critical parameter that influences H_2S removal performance and that a critical crystallite size exists at ~26 nm.

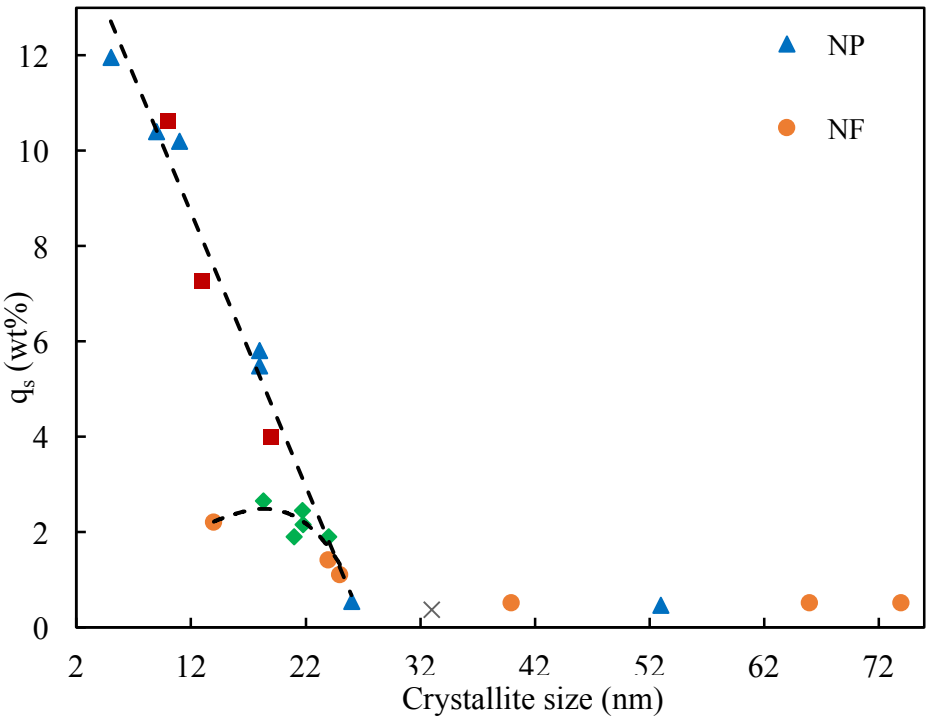

Figure 4. Effect of crystallite size of CuO sorbents prepared via various synthesis techniques as described in **Table S1** on H_2S removal capacity at 1000 ppm-vol H_2S/N_2, 294 K and 1 atm.

TEM images and EDS elemental maps for sulfided NP-1 (5 nm crystals; 12 wt% capacity) and FP-3 (19 nm crystals; 4 wt% capacity) were collected to further probe the length scale that limits H_2S removal capacity. **Figure 5(a)** presents TEM scan of two NP-1 65-75 μm particles after sulfidation at 1000 ppm-vol at 298 K and 1 atm. The scans show nearly spherical particles with some microstructure details in particle 1. The dark areas in particle 1 correspond to unevenly distributed mesopores, and the absence of copper and sulfur in these regions confirms that these areas correspond to voids rather than topographical features. **Figure 5(b-c)** show the corresponding elemental maps for Cu K and S K series derived from EDS spectra. **Figure 5(d)** shows a cross-sectional elemental composition across the indicated line in the TEM image of

particle 2. Again, sulfur appears to follow the same concentration trend as copper throughout the cross section.

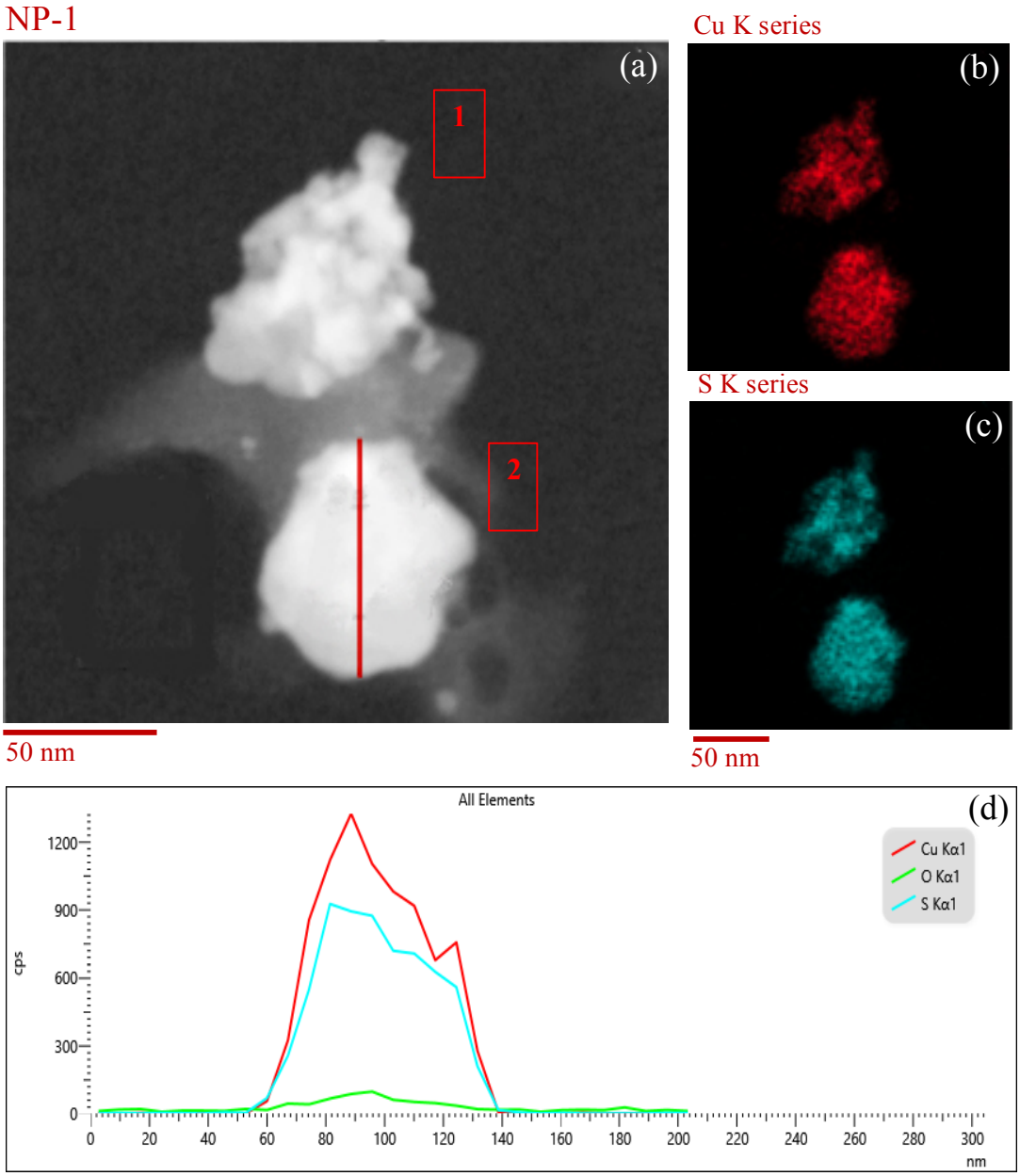

Figure 5. a) TEM image for two 65-75 nm particles of NP-1 sorbent after sulfidation at 1000 ppm-vol H_2S/N_2, 294 K and 1 atm. b) Cu K and c) S K elemental maps for the NP-1 sulfidated particles based on EDS spectra. d) Cross-sectional atomic composition of Cu, S and O K spectra across the length of the particle, indicated by a red line in the TEM scan.

For larger particles of NP-1 (**Figure 6**), the elemental maps and TEM images reveal slight heterogeneity. The TEM image in **Figure 6(a)** features 545-620 nm particles, and the Cu K and S K elemental map (**Figure 6(b-c)**) and EDS analysis across the center of the particle (**Figure 6(d)**) shows that the portion of the particle on the right side of the image is less dense than that on the left side. This density difference may be caused by uneven packing of crystallites within regions of this larger particle, which in turn, leads to the slightly uneven distribution of the elements throughout the volume of the particle as highlighted in **Figure 6**.

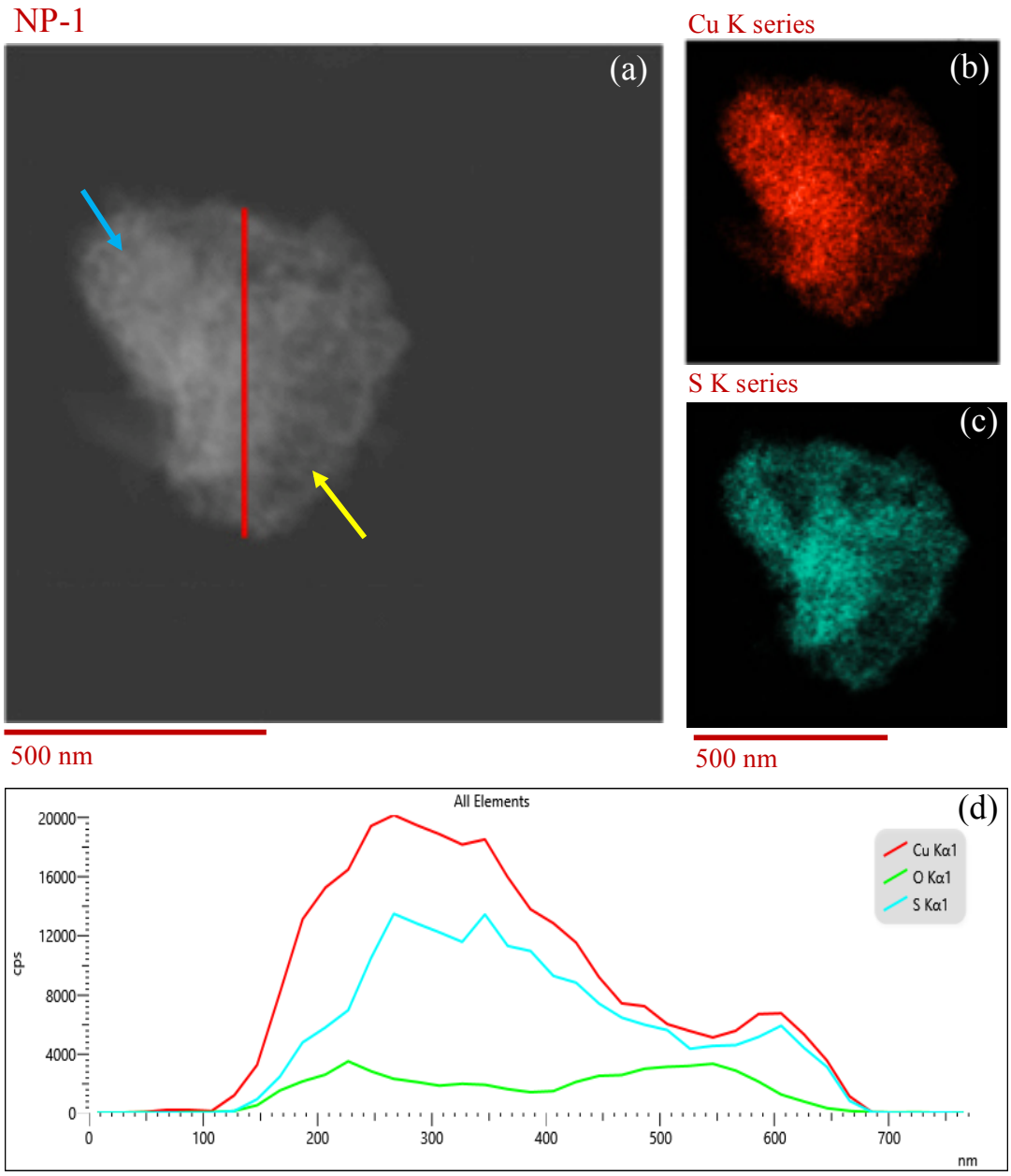

Figure 6. a) TEM image for 545-620 nm particles of NP-1 sorbent after sulfidation at 1000 ppm-vol H_2S/N_2, 294 K and 1 atm. b) Cu K and c) S K elemental maps for the NP-1 sulfidated particles based on EDS spectra. d) Cross-sectional atomic composition of Cu, S and O K spectra across the length of the particle, indicated by a red line in the TEM scan.

Despite these intra-particle heterogeneities, intra-particle regions with similar density exhibited constant Cu and S chemical profiles. Furthermore, Cu K and S K series EDS elemental maps for 55-70 nm particles of sulfided FP-3 (**Figure 7**) also exhibit uniform distributions of Cu and S within the same intra-particle regions, despite the lower ratio of S to Cu in this particle (compared to NP-1).

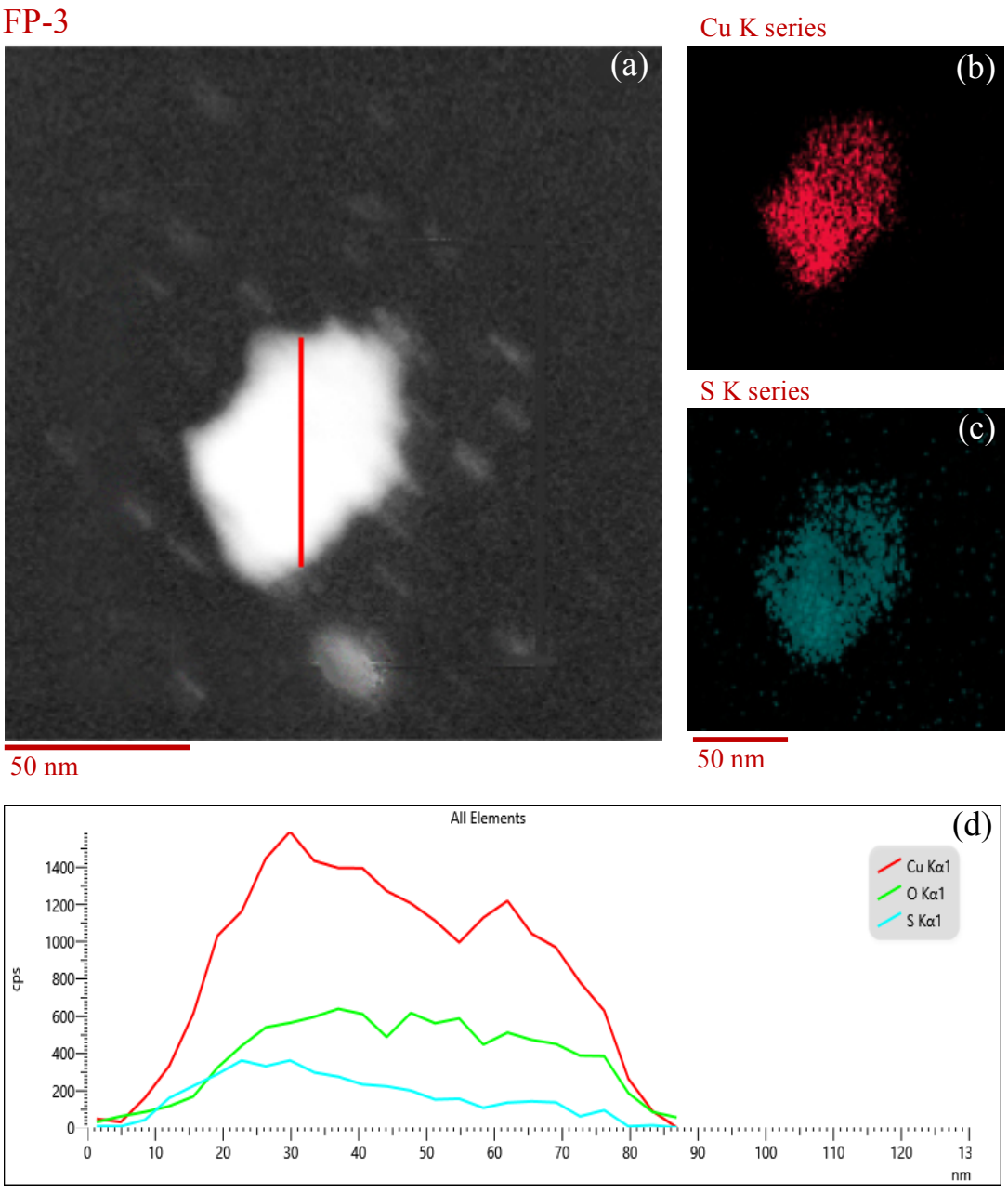

Figure 7. a) TEM image for a 55-70 nm particle of FP-3 after sulfidation at 1000 ppm-vol H_2S/N_2, 294 K and 1 atm. b) Cu K and c) S K elemental maps for the NP-1 sulfidated particles based on EDS spectra. d) Cross-sectional atomic composition of Cu, S and O K spectra across the length of the particle, indicated by a red line in the TEM scan.

The overlapping and homogeneous spatial distributions of copper and sulfur in these particles suggests a homogenous propagation of reaction front throughout particles (>50 nm diameter) that could consist of on the order of 102-6 individual CuO crystallites (of 5-19 nm diameter). These results confirm the most significant influence of H_2S removal in these studies is at the crystallite level (rather than meso-porosity, macro-porosity and/or microscopic morphology), and thus sulfur gradients (implied by the lower than stoichiometric capacities in **Figure 4**) must exist at the CuO crystallite level.

The apparently much stronger influence of crystallite size on sorption capacity (compared to morphology, surface area, and pore structure) may be the result of enhanced constraints for the solid diffusion of atoms across the crystallite as size increases. Previous studies of the sulfidation of ZnO[51] proposed a reaction mechanism consisting of the following general steps:

(1) The dissociative adsorption of H_2S on the particle surface

(2) Nucleation of ZnS on the ZnO surface

(3) Outward diffusion steps of Zn and O vacancies and of O atoms

(4) Vacancy annihilation and water desorption

We propose a similar mechanism for CuO sulfidation in which oxygen and/or copper atoms from the bulk CuO crystal phase diffuse to the reaction interface (step 3 above) after reaction of H_2S molecules with the surface oxygen atoms (step 2 above). The increased crystallite size may hinder this diffusion phenomenon, which is necessary for CuO to fully transform into copper

sulfide (CuS), in two ways: (i) via the formation of thicker CuS layers which lead to a decrease in effective diffusivity values and (ii) via the formation/presence of surface features that are less reactive toward H_2S and its dissociation products.

Sick et al.[52] reported the formation of dense onion-like sulfide layers during CuO sulfidation which dramatically increase solid diffusion resistance by lower values of effective solid phase diffusivities. Increasing crystallite size would require the formation of a thicker outer sulfide layer to achieve the same conversion as a smaller sized crystallite. Indeed, the thickness of this sulfide layer increases with increasing initial CuO crystallite size between 5-20 nm (and up to 4.0 wt% H_2S capacity). These thicker sulfide layers (compared to smaller crystallites) may inhibit the diffusional processes needed for the reaction to proceed to completion.

If sulfide layer thickness was the only phenomenon impeding complete conversion at the crystallite scale, then calculated thickness should be the same for all samples, and the capacity should have a relationship to initial radius that is approximately R^{-1} (see SI). Since the data in **Figure 4** follow a linear trend with R, an additional phenomenon must also impede conversion. As mentioned above, changing crystallite size could also impact the surface features of the reaction interface (e.g., CuO facets) which could change the reaction rates of H_2S molecules and surface species with O and Cu atoms. To probe this molecular explanation for the effect of crystallite size on surface reactivity, our group performed a computational study using Density Functional Theory (DFT) for the reaction between H_2S and CuO surfaces, specifically for the dissociative adsorption of H_2S molecules on a CuO {111} surface.[53] This crystallographic surface is the most stable and common facet of CuO and is the predominant peak in the XRD patterns of the materials tested in this work (see **Figure S2**). CuO {111} surfaces feature two

types of surface O atoms: 3-fold (O_{3c}) and 4-fold (O_{4c}) coordinated. **Figure 8** shows the structure of a CuO {111} surface with these types of atoms.

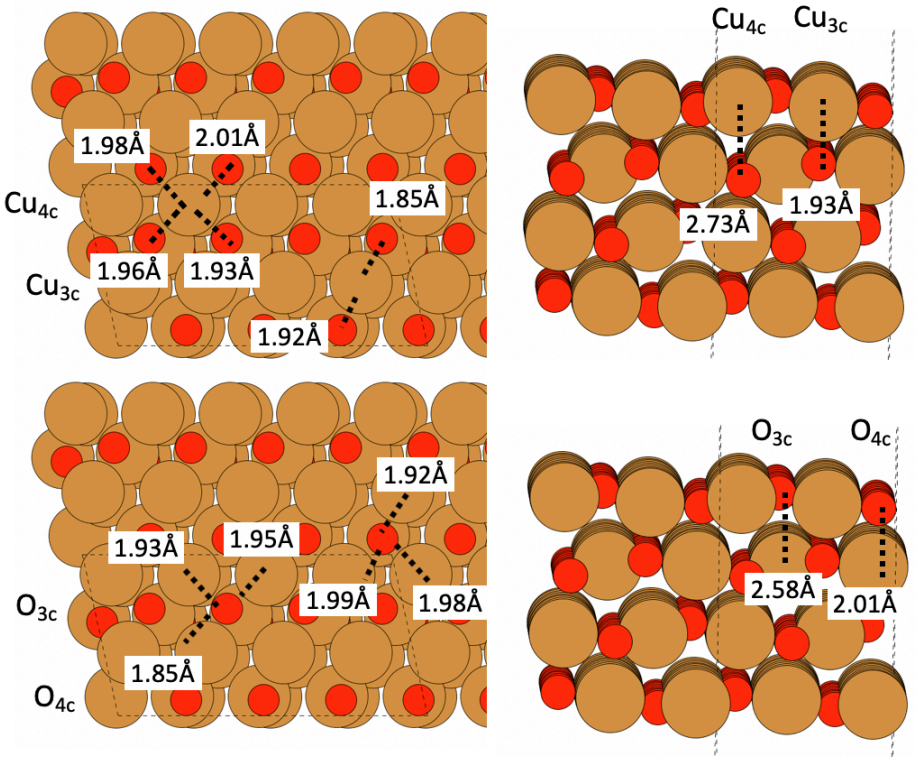

Figure 8: Model of a CuO {111} surface used in this study, showing the different types of surface atoms depending on their condition: O_{3c}/O_{4c} and Cu_{3c}/Cu_{4c} atoms.

These computations revealed that low-coordinated O atoms such as O3c atoms are present to a greater extent for smaller crystallite sizes and that these O3c atoms are more reactive toward adsorbed H_2S: They result in $\Delta G_{T=298K}$ = -106 kJ/mol for the stoichiometric reaction $CuO + x\,H_2S \rightarrow CuO_{1-x}S_x + x\,H_2O$ versus $\Delta G_{T=298K}$ = -52 kJ/mol for O4c atoms. Thus, the higher capacity of CuO materials consisting of smaller crystallites may result from a higher concentration of more reactive O atoms.

In addition to improved reactivity, low coordinated atoms may facilitate diffusion of O atoms via more facile vacancy formation (step 2 above). Previous work by Nolan et al.[54] used DFT to

study the formation of oxygen vacancies on CuO {111} surfaces via vacuum annealing and H_2 reduction. This study observed that formation of vacancies via vacuum annealing from O_{3c} atoms is more favorable than in O_{4c} atoms (E_{vac}=2.77 eV for O_{3c} vs. E_{vac}=3.27 eV for O_{4c}, computed with the hybrid HSE06 functional). The DFT studies in this work also revealed that forming O vacancies by formation of water via H_2 adsorption is favorable ($\Delta E_{ads,T=0K}$= -0.82 eV) for O_{3c} atoms but is unfavorable for O_{4c} atoms ($\Delta E_{ads,T=0K}$= 0.02 eV). This is in agreement with what we found in our computational study, in which the formation of O vacancies via displacement of oxygen atoms by formation of hydroxyl groups proceeds at $\Delta G < 0$ for O_{3c} atoms whereas it does at $\Delta G > 0$ for O_{4c} atoms. Thus, O vacancies may be formed to a much greater extent when the population of low-coordinated O atoms increases (i.e., when crystallite size decreases) which would in turn enhance diffusional processes needed for complete sulfidation. Furthermore, DFT studies showed that upon reaction of the O_{3c} atoms (i.e., replacement with S atoms), the reactivity of the O_{4c} atoms increases because S atoms disrupt the Cu-O bonding states inducing lattice strain: Reaction with O_{4c} atoms in a bare CuO surface results in $\Delta G_{T=298K}$ = -52 kJ/mol, whereas they show $\Delta G_{T=298K}$ = -101 kJ/mol in a partially-sulfided surface in which the outer O_{3c} atoms have been replaced by S atoms. This result implies that as the active O_{3c} atoms in small crystallites react (i.e., leave the lattice), the overall reactivity of the particle is maintained because less reactive O_{4c} atoms become activated for vacancy formation and H_2S reaction. Taken together, these DFT results support a molecular interpretation for the increasing capacity of CuO with decreasing crystallite size that extends beyond a simple diffusion length explanation. Specifically, reaction of low coordinated oxygen (which are predominant on small CuO crystallites) rapidly react with adsorbed H_2S to produce a partially-sulfided surface while also increasing the reactivity of more highly coordinated oxygen atoms. Thus, rates of elementary

reaction and molecular diffusion steps (steps 2 and 3 above) occur more rapidly and to a greater extent on smaller CuO crystallites.

3.4 Influence of carbon-based residues on H_2S removal

Figure 4 also shows a group of samples that deviate from the linear trend of increasing capacity with decreasing crystallite size in the range from 14-24 nm. Namely, decreasing the size of NPC and NF samples, both which involved the use of polymer/surfactant in synthesis, didn't result in an enhancement in the removal capacity compared to other samples in the same crystallite range. The deviation appears to be more pronounced for a nanofiber sample, NF-1, which had a crystallite size of 14 nm which fell well below the trend line, as the removal capacity of this material was merely 2.2 ± 0.1 wt% (compared to 7 wt% for other samples with similar crystallite sizes). As explained in Section 2.2, the synthesis of electrospun nanofibers requires the use of a polymer (PVP or PEO), which upon thermal treatment leaves carbon-based residues on the surface of the material, as discussed in Section 3.1. Thus, this residual carbon, which is undetectable by TGA but apparent on the surface from XPS, influences the reaction in such a manner as to decrease capacity when the crystallite size is less than 20 nm. To further probe the effect of residual C, NF-2 and NF-3 samples were prepared using PVP of different molecular weight, M.W.=1,300,000 and 40,000, respectively. XPS results in **Figure S4** show that the variation in molecular weight didn't affect the amount of residual carbon retained on the surface with 32% C-Cu ratio in NF-2 and 34.9% in NF-3 and it impacted the capacity in the same way. To further investigate the source of poor removal capacity of carbon contaminated samples, NPC-1, NPC-3, NPC-4 and NPC-5 samples were prepared using PVP (M.W.=1,300,000) and a varying polymer to salt ratio (50%, 40%, 20% and 10%). It appears, as shown in **Figure 4**, that the performance of the sorbent fluctuated between 1.9 and 2.4 wt%

regardless of the polymer to salt ratio, and the change in crystallite size in 24-14 nm crystallite size range. **Figure S4** also confirms the same conclusion by showing that the presence of any carbon residue (quantified by XPS results as C-Cu atom%) between (19% and 50%) dampened the performance of the sorbent significantly, in the same way. A plausible explanation for why the presence of any carbon-based residues affects the sorption capacity is due to them blocking the active sites of the reaction, namely the surface oxygen atoms acting as Brønsted basic centers that react with the hydrogen atoms of H_2S molecules and/or the surface copper atoms acting as Lewis acid centers that bond to sulfur atoms. Since the sulfidation process is diffusion-limited (with most of the reaction taking place on grain surfaces) as demonstrated in previous sections, the blocking of any surface-active sites will adversely affect the extent of reaction.

The significance of this observation stems from its relevance to the recent interest in applications of nanofibers in catalytic and chemisorptive processes. Most of the synthesis procedures for nanofibers in literature necessitate the use of polymers in the electrospinning process. Our work shows that the thermal treatment at temperatures as high as 898 K, couldn't get rid of all carbon residue. Increasing the temperature of calcination beyond this point, causes crystal growth which will compromise the performance as well.

4. Conclusions

Several CuO-based nanomaterials were prepared and tested for their performance as low-temperature desulfurizing sorbents by performing fixed-bed sulfidation experiments at ambient temperature and pressure. These materials were prepared via various synthesis techniques, including sol-gel, precipitation, hydrothermal treatment in the presence of a polymer (PVP or PEO) or surfactant (P123), hydrolysis, and electrospinning. A linear driving force model was used to analyze the collected breakthrough curves, to evaluate the removal capacity, qs, and

overall rate parameter, k, for the nineteen sorbents synthesized in this work and glean information about the properties that affect the sorption capacity of unsupported CuO-based sorbents.

Despite differences between the various properties of the tested CuO sorbents as well as their morphologies, a strong linear relationship was recognized between the sorbents' sulfur removal capacity and crystallite size, particularly when the crystallite size of CuO was below 26 nm. It was also observed that CuO materials with crystallite sizes larger than 26 nm had negligible sulfur uptake capacities (~0.5 wt%). The effect of residual carbon was also investigated, and it was found that carbon residues resulting from the use of a polymer (PVP or PEO) or a surfactant (P123) in the synthesis procedure remained on the surface of the sorbent after thermal treatment and detrimentally effected its H_2S uptake capacity. The results in this paper demonstrate the strong influence of crystallite size of unsupported CuO sorbents and their purity on H_2S removal capacity at ambient conditions, irrespective of morphology and other physiochemical properties, such as surface area, pore size, and pore volume. An atomic scale explanation of the strong influence of crystallite size is proposed from model DFT calculations, explaining how elementary reaction and molecular diffusion steps occur more rapidly and to a greater extent on smaller CuO crystallites.

SUPPORTING INFORMATION

Synthesis Methods, Sulfidation Tests, X-Ray Diffraction Patterns, Pore Distribution Curves, Parameters Affecting Carrying Capacity, Sulfidation Test Results

AUTHOR INFORMATION

Corresponding Author

*Corresponding author. Phone: 310-267-0169. Email: dasimonetti@ucla.edu

Author Contributions

The manuscript was written through contributions of all authors. All authors have given approval to the final version of the manuscript. ‡These authors contributed equally.

Funding Sources

The authors acknowledge financial support from the Henry Samueli School of Engineering and Applied Sciences and the Office of Equity, Diversity, and Inclusion at UCLA.

ACKNOWLEDGMENT

The authors acknowledge the Molecular & Nano Archaeology (MNA) Laboratory at UCLA Materials Science Department for use of the SEM, the Electron Imaging Center for NanoMachenes (EICN) at UCLA for use of the TEM, the J.D. McCullough Laboratory of X-ray Crystallography at UCLA Chemistry Department for use of the XRD, the Molecular Instrumentation Center (MIC) at UCLA for use of the TGA and XPS, and Dr. Kodambaka's lab at UCLA for access to and assistance with STM. The authors acknowledge Fang Lui and Luke Minardi's assistance in XPS data collection and analysis. Faisal Alshafei acknowledges Aramco R&D for financially supporting him in his graduate studies at UCLA.

REFERENCES

(1) Cui, H.; Turn, S.Q; Reese, M.A. Removal of sulfur compounds from utility pipelined synthetic natural gas using modified activated carbons. *Catal. Today*. **2009,** *139*, 274-279.

(2) Bandosz, T.J. The Sulfur Problem: Cleaning Up Industrial Feedstocks. *J. Am. Chem. Soc*. **2001,** *123* (3), 516.

(3) Song, C. An overview of new approaches to deep desulfurization for ultra-clean gasoline, diesel fuel and jet fuel. *Catal. Today*. **2003,** *86,* 211-263

(4) Goodwin, M. J.; Musa, O. M.; Steed, J. W. Problems Associated with Sour Gas in the Oilfield Industry and Their Solutions. *Energy & Fuels*. **2015,** *29,* 4667-4682.

(5) Beauchamp, R. O.; Bus, J. S.; Popp, J. A.; Boreiko, C. J.; Andjelkovich, D. A.; Leber, P. A critical review of the literature on hydrogen sulfide toxicity. *CRC Crit. Rev. in Toxicol.* **1984**, *13,* 25-97.

(6) Likens, G. E.; Wright, R. F.; Galloway, J. N.; Butler, T. J. Acid Rain. *Sci. Am.* **1979,** *241* (4), 43-51.

(7) Nasri, N. S.; Jones, J. M.; Dupont, A.; Williams, A. Kinetic Rate Comparison of Methane Catalytic Combustion of Palladium Catalysts Impregnated onto γ-Alumina and Bio-Char *Energy & Fuels*. **1998,** *12,* 1130-1134.

(8) Rosso, C.; Galletti, M.; Bizzi, Saracco, G.; Specchia, V. Zinc Oxide Sorbents for the Removal of Hydrogen Sulfide from Syngas*Ind. Eng. Chem. Res.* **2003**, *42*, 1688–1697.

(9) Rasi, S.; Läntelä, J.; Rintala, J. Trace Compounds Affecting Biogas Energy Utilisation—A Review. *Energy Conversion and Management*. **2011**, *52* (12), 3369-3375.

(10) Balichard, K.; Nyikeine, C.; Bezverkhyy, I. Nanocrystalline $ZnCO_3$-A novel sorbent for low-temperature removla of H_2S. *J. Hazard. Mater*. **2014**, *264*, 79–83.

(11) Kang, S.-H.; Bae, J. W.; Kim, S.-M.; Jun, K.-W. Effect of Phosphorus Modification on Cu–ZnO–Al_2O_3 for the Removal of H_2S. *Energy & Fuels*. **2008**, *22* (4), 2580-2584.

(12) Montes, D.; Tocuyo E.; Gonzálex, E.; Rodríguez, D.; Solano, R.; Ramos, M. A.; Moronta, A. Reactive H_2S chemisorption on mesoporous silica molecular sieve-supported CuO or ZnO. *Microporous and Mesoporous Materials*. **2013,** *168,* 111-120.

(13) Elyassi, B.; Al Wahedi, Y.; Rajabbeigi, N.; Kumar, P.; Jeong, J. S.; Zhang, X.; Balasubramanian, V. V; Katsiotis, M. S.; Andre Mkhoyan, K; Al Hashimi, S.; Tsapatsis, M. A high-performance adsorbent for hydrogen sulfide removal *Microporous and Mesoporous Materials*. **2014,** *190,* 152-155.

(14) Pineda, M.; Palacios, J M.; Alonso, L.; García, E.; Moliner, R. Performance of zinc oxide based sorbents for hot coal gas desulfurization in multicycle tests in a fixed-bed reactor. *Fuel*. **2000,** *79,* 885-895.

(15) Bagajewicz, M. J.; Tamhankar, S. S.; Stephanopoulos, M. F.; Gavalas, G. R. Hydrogen sulphide removal by supported vanadium oxide. *Environ. Sci. Technol.* **1998**, *22*, 467-470.

(16) Chauk, S. S.; Agnihotri, R.; Jadhav, R. A.; Misro, S. K.; Fan, L.-S. Kinetics of high-pressure removal of hydrogen sulfide using calcium oxide powder. *AIChE J.* **2000,** *46,* 1157-1167.

(17) Baird, T.; Denny, P. J.; Hoyle, F.; McMonagle, D. Modified Zinc-Oxide Absorbents for Low-Temperature Gas Desulfurization. *J. Chem. Soc., Farady Trans.* **1992,** *88,* 3375-3382.

(18) Karvan, O.; Atakül, H. Investigation of CuO/mesoporous SBA-15 sorbents for hot gas desulfurization. *Fuel Process. Technol.* **2008**, *89*, 908–915.

(19) Jiang, D.; Su, L.; Ma, L.; Yao, N.; Xu, X.; Tang, H.; Li, X. Cu–Zn–Al mixed metal oxides derived from hydroxycarbonate precursorsfor H_2S removal at low temperature. *Appl. Surf. Sci.* **2010**, *256*, 3216–3223.

(20) Sánchez, J. M.; Ruiz, E.; Otero, J. Selectove removal of hydrogen sulphide from gaseous streams using a zinc-based sorbent. *Ind. Eng. Chem. Res.* **2005**, *44*, 241–249.

(21) Barin, I.; Kubaschewski, O.; Knacke, O. *Thermochemical Properties of Inorganic Substances;* Springer-Verlag: Düsseldorf 1977; pp 861.

(22) Balsamo, M.; Cimino, S.; de Falco, G.; Erto, A.; Lisi, L. ZnO-CuO supported on activated carbon for H_2S removal at room temperature. *Chem. Eng. J.* **2016**, *304*, 399–407.

(23) Karvan, O.; Sirkecioğlu, A.; Atakül, H. Investigation of nano-CuO/mesoporous SiO_2 materials as hot gas desulphurization sorbents. *Fuel Process. Technol.,* **2009**, *90*, 1452–1458.

(24) Ko T.-H.; Chu H.; Chaung, L.-K. The sorption of hydrogen sulfide from hot syngas by metal oxides over supports. *Chemosphere*. **2005**, *58*, 467–474.

(25) Yasyerli, S.; Dogu, G.; Ar, I.; Dogu, T. Activities of copper oxide and Cu–V and Cu–Mo mixed oxides for H_2S removal in the presence and absence of hydrogen and predictions of a deactivation model. *Ind. Eng. Chem. Res.* **2001**, *40*, 5206–5214.

(26) Li, Z.; Flytzani-Stephanopoulos, M. Cu-Cr-O and Cu-Ce-O regenerable oxide sorbents for hot gas desulfurization. *Ind. Eng. Chem. Res.* **1997**, *36*, 187–196.

(27) Carnes, C. L.; Klabunde, K. J. Unique Chemical Reactivities of Nanocrystalline Metal Oxides toward Hydrogen Sulfide. *Chem. Mater.* **2002**, *14*, 1806–1811.

(28) Kayani, Z. N.; Umer, M.; Riaz, S.; Naseem, S. Characterization of Copper oxide nanoparticles fabricated by the Sol–Gel Method. *J. Electron. Mater.* **2015**, *44*, 3704–3709.

(29) Zhu, J.; Bi, H.; Wang, Y.; Wang, X.; Yang, X.; Lu, L. Synthesis of flower-like CuO nanostructures via a simple hydrolysis route. M *Mater. Lett.,* **2007**, *61*, 5236–5238.

(30) Huang, J.; Tang, F.; Gu, C.; Shi, C.; Zhai, M. Flower-like CuO hierarchical nanostructures: synthesis, characterization, and property. *Front. Optoelectron.* **2012**, *5*, 429–434.

(31) Liu, C.; Zhang, L.; Deng, J.; Mu, Q.; Dai, H.; He, H. Surfactant-Aided Hydrothermal Synthesis and Carbon Dioxide

(32) Adsorption Behavior of Three-Dimensionally Mesoporous Calcium Oxide Single-Crystallites with Tri-, Tetra-, and Hexagonal Morphologies. *J. Phys. Chem. C.* **2008**, *112*, 19248–19256.

(33) Yu, J. C.; Xu, A.; Zhang, L.; Song, R.; Wu, L. Synthesis and Characterization of Porous Magnesium Hydroxide and Oxide Nanoplates. *J. Phys. Chem. B.* **2004**, *108*, 64–70.

(34) Biesinger, M. C.; Lau, L. W. M.; Gerson, A. R.; Smart, R. S. C. Resolving surface chemical states in XPS analysis of first row transition metals, oxides and hydroxides: Sc, Ti, V, Cu and Zn. *Appl. Surf. Sci.* **2010**, *257*, 887–898.

(35) Hu, J.; Li, D.; Lu, J. G.; Wu, R. Effects on electronic properties of molecule adsorption on CuO surfaces and nanowires. *J. Phys. Chem. C*. **2010,** *114* (40), 17120–17126.

(36) Kresse, G.; Hafner, J. Ab initio molecular dynamics for liquid metals. *Physical Review B*. **1993,** *47*, 558.

(37) Kresse, G.; Hafner, J. Ab initio molecular-dynamics simulation of the liquid-metal–amorphous-semiconductor transition in germanium. *Physical Review B*. **1994,** *49* (20), 14251.

(38) Kresse, G.; Furthmüller, J. Efficiency of ab-initio total energy calculations for metals and semiconductors using a plane-wave basis set. *Computational materials science*. **1996,** *6* (1). 15-50.

(39) Kresse, G.; Furthmüller, J. Efficient iterative schemes for ab initio total-energy calculations using a plane-wave basis set. *Physical review B*. **1996,** *54* (16). 11169.

(40) Perdew, J. P.; Burke, K.; Ernzerhof, M. Generalized Gradient Approximation Made Simple. *Physical review letters*. **1996,** *77* (18), 3865.

(41) Wang, L.; Maxisch, T.; Ceder, G. Oxidation energies of transition metal oxides within the GGA + U framework *Physical Review B*. **2006,** *19,* 195107.

(42) Zhang, Q.; Zhang, K.; Xu, D.; Yang, G.; Huang, H.; Fude, N.; Liu, C.; Yang, S. CuO nanostructures: Synthesis, characterization, growth mechanisms, fundamental properties, and applications. *Progress in Materials Science*. **2014,** *60,* 208-337.

(43) Nolan, M.; Elliott, S. D. The p-type conduction mechanism in Cu_2O: a first principles study. *Physical Chemistry Chemical Physics*. **2006,** *8* (45), 5350–5358.

(44) Su, D.; Xie, X.; Dou, S.; Wang, G. CuO single crystal with exposed {001} facets - A highly efficient material for gas sensing and Li-ion battery applications. *Sci. Rep*. **2014**, *4*, 5753.

(45) Mohan, V. M.; Raja, V.; Sharma, A. K.; Narasimha Rao, V. V. R. Ion transport and battery discharge characteristics of polymer electrolyte based on PEO complexed with NaFeF4 salt, Ionics (Kiel). *Ionics (Kiel)*. **2006**, *12*, 219.

(46) Aguirre, J. M.; GutiÃrrez, A.; Giraldo, O. Simple Route for the Synthesis of Copper Hydroxy Salts. *J. Braz. Chem. Soc*. **2011**, *22*, 546–551.

(47) Zhang, Q.; Zhang, K.; Xu, D.; Yang, G.; Huang, H.; Fude, N.; Liu, C.; Yang, S. CuO nanostructures: Synthesis, characterization, growth mechanisms, fundamental properties, and applications. *Progress in Materials Science*. **2014,** *60,* 208-337.

(48) Borodko, Y.; Lee, H. S.; Joo, S. H.; Zhang, Y.; Somorjai, G. Spectroscopic Study of the Thermal Degradation of PVP-Capped Rh and Pt Nanoparticles in H_2 and O_2 Environments. *J. Phys. Chem. C*. **2010**, *114*, 1117–1126.

(49) Kozak, D. S.; Sergiienko, R. A.; Shibata, E.; Iizuka, A.; Nakamura, T. Non-electrolytic synthesis of copper oxide/carbon nanocomposite by surface plasma in super-dehydrated ethanol. *Sci. Rep*. **2016**, *6*, 21178.

(50) Biljana, Š.; Banks, C. E.; Alison, C.; Compton, R. G. Iron(III) Oxide Graphite Composite Electrodes: Application to the Electroanalytical Detection of Hydrazine and Hydrogen Peroxide. *Electroanalysis*. **2006,** *19*, 79–84.

(51) Neveux, L.; Chiche, D.; Bazer-Bachi, D.; Favergeon, L.; Pijolat, M. New insight on the ZnO sulfidation reaction: Evidences for an outward growth process of the ZnS phase. *Chemical Engineering Journal*. **2012,** *181*, 508–515.

(52) Sick, G.; Schwerdtfeger, K. Hot desulfurization of coal gas with copper. *Metallurgical Transactions B*. **1987,** *18* (3), 603-609.

(53) "On the mechanism of reactive sorption of H_2S on CuO 111 surfaces - A first-principles study." Manuscript under preparation.

(54) Maimaiti, Y.; Nolan, M.; Elliott, S. D. Reduction mechanisms of the CuO (111) surface through surface oxygen vacancy formation and hydrogen adsorption. *Phys. Chem. Chem. Phys*. **2014,** *16* (7), 3036-3046.

TOC Graphic

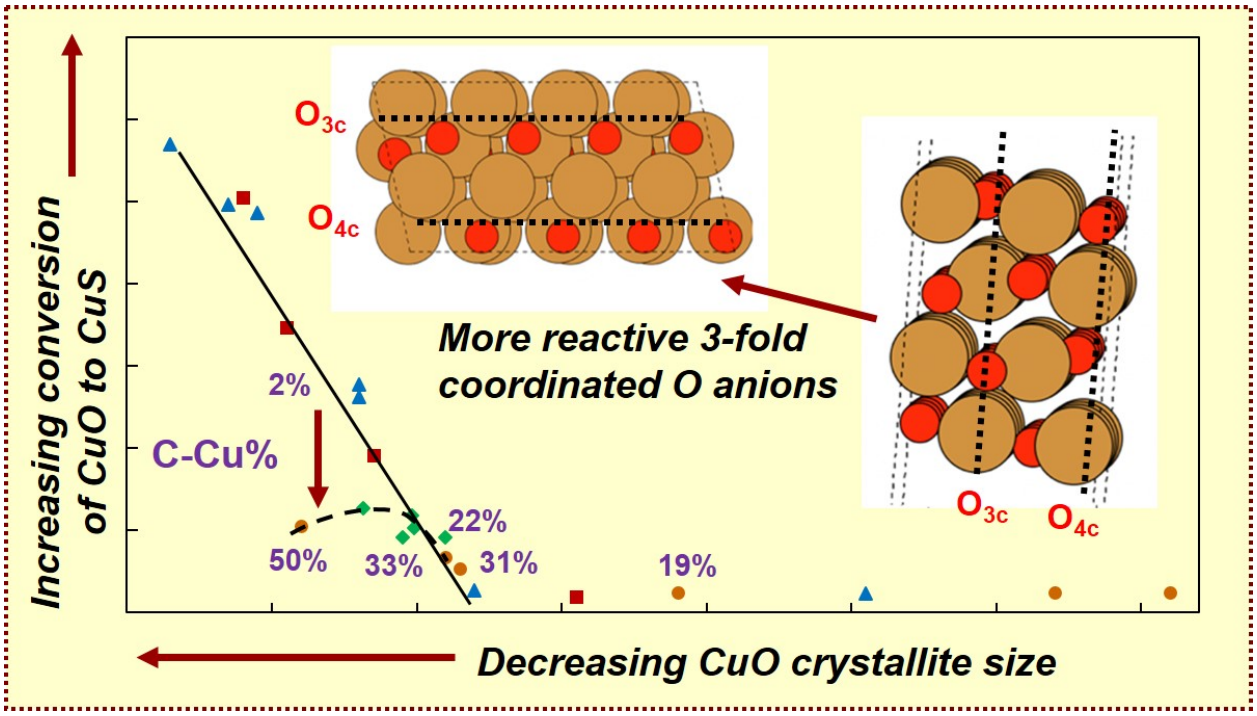
Increasing conversion of CuO to CuS
O3c
O4c
More reactive 3-fold coordinated O anions
2%
C-Cu%
50%
33%
22%
31%
19%
O3c
O4c
Decreasing CuO crystallite size